

RSC Advances



This is an *Accepted Manuscript*, which has been through the Royal Society of Chemistry peer review process and has been accepted for publication.

Accepted Manuscripts are published online shortly after acceptance, before technical editing, formatting and proof reading. Using this free service, authors can make their results available to the community, in citable form, before we publish the edited article. This *Accepted Manuscript* will be replaced by the edited, formatted and paginated article as soon as this is available.

You can find more information about *Accepted Manuscripts* in the [Information for Authors](#).

Please note that technical editing may introduce minor changes to the text and/or graphics, which may alter content. The journal's standard [Terms & Conditions](#) and the [Ethical guidelines](#) still apply. In no event shall the Royal Society of Chemistry be held responsible for any errors or omissions in this *Accepted Manuscript* or any consequences arising from the use of any information it contains.

ARTICLE

Highly efficient removal of NO with ordered mesoporous manganese oxide at low temperature

Cite this: DOI: 10.1039/x0xx00000x

Sihui Zhan,^{*a,b} Dandan Zhu,^a Mingying Qiu,^a Hongbing Yu,^a Yi Li^{*c}

Received 00th January 2014,
Accepted 00th January 2014

DOI: 10.1039/x0xx00000x

www.rsc.org/

Highly ordered mesoporous MnO₂ has been prepared using KIT-6 as hard template for the selective catalytic reduction (SCR) activity of NO with NH₃ at low temperature, which was characterized by TEM, XRD, BET, XPS, H₂-TPR, NH₃-TPD and in-situ DRIFT. Based on the result of HRTEM, the ordered mesoporous channels of MnO₂ can be clearly observed. Moreover, the SCR activity of NO with NH₃ at low temperature was evaluated using these ordered mesoporous MnO₂ as catalyst, it can be found that 100% NO conversion efficiency can be reached from 150 to 250°C. As comparison, mesoporous Mn₂O₃ and bulk MnO₂ have been synthesized and used to test their NO conversion at the same parameters. Furthermore, its mechanism of improved SCR performance has been investigated, and it is indicated that specific surface area, surface chemisorbed oxygen, reducibility and acid sites have great effect on the SCR reaction based on results of XPS, H₂-TPR, NH₃-TPD and in situ DRIFT. In addition, the effect of H₂O and GHSV on NO conversion has been investigated.

Keywords: Ordered mesoporous, MnO₂, Low temperature, SCR

ARTICLE

1 Introduction

Nitrogen oxides (NO) originated in industrial combustion of coal and fossil fuel can result in a series of serious effects on atmospheric environment, such as photo-chemical smog, acid rain and ozone depletion, which have drawn widely concern due to its high toxicity to human health^{1,2}. Among many approaches for removing NO, selective catalytic reduction (SCR) degradation of NO with NH₃ is considered as one of the most efficient and widely used methods. Until now, the commercial V₂O₅-WO₃/TiO₂ catalysts are used in the SCR field, however, its higher working temperature from 300 to 400 °C resulted that the reaction device of SCR unit has to be located at upstream of electrostatic precipitator, which will bring a lot of problems, such as inactivation, catalyst agglomeration and higher cost^{3,4}. Furthermore, in order to avoid these drawbacks, it is necessary to preheat the flue gas higher than 200 °C if we want to locate the VWTi SCR reactor in downstream of electrostatic precipitator. Therefore, it is urgent to develop novel low-temperature SCR catalyst to overcome these problems.

According to the previous reports, Mn-based catalysts proved to show excellent SCR activity at low temperature by doping transition metal oxides into MnOx, such as MnOx/CeO₂⁴, MnOx/TiO₂⁵, MnOx/CuO^{6,7} and MnOx/Fe⁸, and so on. However, the SCR activity of pure MnO₂ was poor, and no corresponding research has been done to improve its degradation efficiency. As we all know, the SCR removal performance of NO can be obviously affected by the oxidation state of manganese, the crystallinity and the specific surface⁹. For example, Yang found that MnO₂ nanorods performed the higher activity for reducing NO than MnO₂ nanotubes and nanoparticles, which is due to its low crystallinity, more lattice oxygen, high reducibility, and stronger acid sites¹⁰.

Since the discovery of MCM-41 and SBA-15, mesoporous materials are attracting more and more widespread concerns due to their large specific surface area, interconnected channels and well defined pore diameters^{11,12}. It is found that these hierarchical structures are beneficial for the generation of abundant active sites and mass transfer, enabling the effective reduction of NO¹³⁻¹⁵. Recently, mesoporous MnO₂ has been prepared and applied in many fields such as lithium-ion batteries¹⁶, supercapacitors¹⁷ and catalytic domain¹⁸. However, to our knowledge, there is no report to use mesoporous MnO₂ for SCR removal of NO with NH₃ at low temperature.

In this paper, the highly ordered pure mesoporous MnO₂ was successfully prepared through nanocasting method using KIT-6 as template, which was characterized by TEM, XRD, BET, H₂-TPR, NH₃-TPD, XPS and in-situ DRIFT. In addition, the SCR activity of NO with NH₃ at low temperature was evaluated using these ordered mesoporous MnO₂ as catalyst. Furthermore, mesoporous Mn₂O₃ and bulk MnO₂ nanoparticles were prepared and used as SCR catalyst to clean NO with NH₃, and the reaction mechanism has been suggested.

2 Experimental

2.1 Materials

All chemicals used here are analytical grade. The KIT-6 was prepared based on earlier published paper¹⁹. Hydrochloric acid (HCl), ethanol, N-butanol, sodium hydroxide (NaOH), tetraethyl orthosilicate (TEOS) were purchased from Jiangtian Chemical Technology Co. Ltd. (Tianjin, China). Both Pluronic P123 and Mn(NO₃)₂·4H₂O(97%) were purchased from Sigma-Aldrich.

2.2 Catalyst preparation

The highly ordered mesoporous MnO₂ was prepared using mesoporous silica KIT-6 as a template²⁰. In a typical process, 3g of Mn(NO₃)₂·4H₂O (97%) was dissolved in 25 mL of ethanol, and then 1g of KIT-6 was added to the above solution. The mixture was stirred overnight at room temperature, the powder sample was then sintered in a muffle furnace with a heating rate of 1 °C/min from room temperature to 350 °C and maintained at 350 °C for 5 h. After cooling to room temperature, the resulting powder was treated twice with a hot aqueous solution of 2M NaOH to remove the silica template, followed by washing with deionized water several times and then dried at 60 °C.

The synthesis process of ordered mesoporous Mn₂O₃ was similar with MnO₂, and the only difference between Mn₂O₃ and MnO₂ was that the obtained solid was calcined in a muffle furnace with a heating rate of 1 °C/min from room temperature to 600 °C and maintained at 600 °C for 4 h.

As a comparison, the conventional MnO₂ was prepared directly by calcining Mn(NO₃)₂·4H₂O (97%) at 350 °C for 5 h.

2.3 Characterization

The size and morphology of MnO₂ and Mn₂O₃ were observed by transmission electron microscopy (TEM) using a JEOL Model JEM-1200EX at 80 kV. The X-ray diffraction (XRD) patterns of MnO₂ were recorded via an X-ray diffractometer (Rigaku D/Max 2200PC) with a graphite monochromator and CuK α radiation ($\lambda=0.15418$ nm) at room temperature, with the voltage and electric current being fixed at 28 kV and 20 mA. N₂ adsorption-desorption isotherms were recorded via Quantachrome AutoSorb iQ-MP. Temperature-programmed reduction of H₂ (H₂-TPR) and temperature-programmed desorption of NH₃ (NH₃-TPD) were carried out on a Micromeritics Autochem 2920 II instrument with the thermal conductivity detector (TCD). The oxidation state and concentration of sample surface were observed using X-ray photoelectron spectroscopy (XPS, ESCALAB 250 multi-technique X-ray photoelectron spectrometer (UK)), with a monochromatic AlK α X-ray source ($h\nu=1486.6$ eV). All XPS spectra were recorded using an aperture slot of 300*700 microns, survey spectra were recorded with a pass energy of 160 eV, and high resolution spectra with a pass energy of 40 eV. The in situ Diffuse Reflectance Infrared Fourier Transform Spectroscopy (in situ DRIFTS) spectra were recorded using a Bruker Tensor 27 spectrophotometer. Prior to each experiment, the sample was heated to 350°C in argon for 1h and then cooled to 150°C. The spectra were recorded using KBr pellet method in the range of 400-4000 cm⁻¹ by accumulating 32 scans at a resolution of 4 cm⁻¹.

2.4 Catalytic activity test

The SCR activity measurements were carried out in fixed-bed quartz reactor (i.d. 10 mm), operating under atmospheric pressure at 100-350 °C. For each SCR activity test, 0.5g of catalysts were used (pressed into blocks, and then crushed and sieved into 40-60 meshes before SCR activity measurements). The typical reaction conditions were set as follows: 0.5 g catalyst, 500 ppm NO, 500 ppm NH₃, 3% O₂, 5% H₂O (when used), all balanced by N₂ with a total gas flow rate of 200mL/min, giving a gas hourly space velocity (GHSV) of 2.8×10⁴ h⁻¹. The gas-phase concentrations of all components were measured by a FTIR spectrometer (Gasmeter FTIR DX4000, Finland). The NO conversion under steady-state reaction condition for 1 h was obtained from the following equation, in which NO_{in} was the concentration of inlet NO, and NO_{out} was the concentration of outlet NO:

$$\text{NO conversion (\%)} = (1 - [\text{NO}]_{\text{out}} / [\text{NO}]_{\text{in}}) \times 100\%$$

3 Results and discussion

3.1 Characterization of catalyst

To study the microstructure of MnO₂ in detail, the typical TEM images with different magnifications were shown in Figure 1, indicating that the cubic mesostructure and lattice fringe of MnO₂ can be directly observed. From Figure 1a-c, the 6.7 nm average pore diameter of MnO₂ (Figure b-c) are consistent with the 5.9 nm wall thickness of KIT-6 (Figure 1a), which indicates that cubic mesostructures of MnO₂ result from the thermal decomposition of metal precursors within the confined mesochannels of the silica template^{20,21}. Besides, the unit cell parameters, $a0$, are 11.2 and 22.8nm for mesoporous MnO₂ and Mn₂O₃. As illustrated in the typical HRTEM image of MnO₂ (Figure 1d), lattice fringes of MnO₂ that belong to the (110) crystallographic planes ($d=0.341$ nm) and the (101) crystallographic planes ($d=0.254$ nm) can be found out clearly, demonstrating that MnO₂ sample is highly crystalline. Furthermore, the electron diffraction patterns of MnO₂ sample can be indexed to the highly crystalline reflections, which is in accordance with the below result of XRD. Compared the TEM image of mesoporous MnO₂ (Figure 1c) with mesoporous Mn₂O₃ (Figure 1e), the order of mesoporous MnO₂ is better than mesoporous Mn₂O₃, which may be due to the incomplete pore filling of precursor and the relative large volume shrinkage during the sintering process and is consistent with the result of XRD below^{21,22}. To evaluate the stability of mesostructure materials, the characterization of TEM for the used mesoporous MnO₂ was conducted, as shown in the Figure 1f. It is obviously observed that the used mesoporous MnO₂ still show highly ordered mesoporous channels after SCR test, which confirmed clearly the high stability of mesoporous MnO₂. In addition, energy dispersive X-ray spectroscopy (EDS) was also conducted to analyze the chemical composition of MnO₂, which obviously proved that MnO₂ catalysts were composed with Mn and O elements. And, the existence of C and Cu peak in EDS spectrum come from the copper mesh used in TEM tests and the little existence of element Si originate from residues of KIT-6 template.

To further study the mesostructure of samples, low-angle XRD patterns of mesoporous MnO₂ and Mn₂O₃ are shown in Figure 2a. As shown in Figure 2a, the characteristic reflection of (211) plane at

ARTICLE

2θ of around 1° for mesoporous MnO_2 can be observed clearly, corresponding to the main (211) diffraction peak of the cubic Ia 3d symmetry of mesoporous silica template (Figure 1S), which indicates the highly ordered mesoporous structure of MnO_2 ²³. Besides, the broad peak at $1.7\text{--}1.8^\circ$ indexed as (332) plane for mesoporous MnO_2 further demonstrates the relatively ordered mesostructure, which is in good agreement with above TEM result. For mesoporous Mn_2O_3 , the characteristic reflection of (211) plane at 2θ value around 1° also can be observed clearly, indicating mesoporous Mn_2O_3 has been prepared successfully. However, their positions had shifted toward higher angles and there are no other diffraction peaks, suggesting that the mesostructure of Mn_2O_3 is less ordered than mesoporous MnO_2 , which may be due to the incomplete pore filling of precursor and the relative large volume shrinkage during the sintering process^{21,22}. Besides, the d-values calculated from the first peak are 92.9 and 84.9 Å, which correspond to the unit cell parameters, $a0$, 10.7 and 22.4 nm for mesoporous MnO_2 and Mn_2O_3 , respectively. These values are in good agreement with the TEM results^{22,24}.

Wide-angle XRD patterns of bulk MnO_2 , mesoporous MnO_2 and Mn_2O_3 are shown in Figure 2b. From Figure 2b, peak positions of mesoporous MnO_2 are same with bulk MnO_2 . However, the diffraction peaks of mesoporous MnO_2 are broader and lower than bulk MnO_2 due to the very fine grain size and defect along the channel produced in the decomposition process, suggesting that the obtained mesoporous MnO_2 are nano-size. And, the diffraction peaks of both bulk MnO_2 and mesoporous MnO_2 can be well indexed to MnO_2 (JCPDS 24-0735)²². The diffraction peaks of mesoporous Mn_2O_3 can be well indexed to pure Mn_2O_3 (JCPDS 24-0508)²⁴. For both mesoporous MnO_2 and Mn_2O_3 , no peaks from other phases have been detected, suggesting that the synthesized mesoporous MnO_2 and Mn_2O_3 are of high purity. By the way, the average particle size is about 36.4nm for bulk MnO_2 based on the Scherrer equation, while the average particle size of mesoporous MnO_2 and mesoporous Mn_2O_3 is about 7.2nm and 13 nm respectively.

The N_2 adsorption-desorption isotherms and the pore diameter distribution of the mesoporous MnO_2 , mesoporous Mn_2O_3 and bulk MnO_2 are shown in Figure 3, and the data of the pore size distribution, pore volume, and surface area are listed in Table 1. As shown in Figure 3a, the typical IV type isotherms of mesoporous MnO_2 and mesoporous Mn_2O_3 in the relative pressure ranging from 0.4 to 0.8 for are characteristic of mesostructure with the quality of

pores inferior to KIT-6 template, which are in good agreement with the results observed TEM and XRD^{25,26}. In addition, a small hysteresis loop in the relative pressure ranging from 0.8 to 1.0 for mesoporous MnO_2 and mesoporous Mn_2O_3 can be also observed, indicating the presence of a small amount of macropores that might originate from the voids between the ordered mesoporous entities²⁵. However, the bulk MnO_2 didn't exhibit the typical IV type isotherm, indicating that the bulk MnO_2 has not mesoporous channels. Based on the datas shown in Fig. 3b, it can be concluded that the pore size distribution of all of the samples is uniform and centered on 3.8 nm.

As shown in Table 1, the mesoporous MnO_2 with a surface area of 129.274 m^2/g and a pore volume of 0.203 cc/g are much larger than those of bulk MnO_2 with a surface area of 5.589 m^2/g and a pore volume of 0.006 cc/g . The mesoporous Mn_2O_3 with a surface area of 78.724 m^2/g and a pore volume of 0.068 cc/g are lower than mesoporous MnO_2 , which might originate from the collapse of mesostructure caused by the incomplete pore filling of precursor and the relative large volume shrinkage under a higher calcination temperature of Mn_2O_3 ²¹⁻²³.

As we all know, the surface acidity of catalyst plays a very important role in low temperature SCR of NO with NH_3 ²⁷. Therefore, to evaluate the acidic sites distribution, NH_3 -TPD patterns of mesoporous MnO_2 , mesoporous Mn_2O_3 and bulk MnO_2 were carried out, separately (Figure 4a). Due to the thermal stability of the NH_3 molecules coordinated to the Lewis acid sites was higher than the NH_4^+ ions bound to the Brønsted acid sites, it can be deduced that desorption peak at low temperature (below 200°C) is assigned to NH_4^+ ions bound to Brønsted acid sites and the desorption peaks at high temperature is associated with coordinated NH_3 molecules originating from the Lewis acid sites²⁷. Therefore, for bulk MnO_2 , the single main peak ranging from 450 to 550°C indicates a distribution of medium acid sites, which is attributed to the coordinated NH_3 molecules originating from the Lewis acid sites²⁸. Three NH_3 -TPD peaks of mesoporous MnO_2 can be observed obviously. The desorption peak at low temperature ranging from 150 to 200°C is due to the NH_4^+ ions bound to Brønsted acid sites from weak and medium acid sites distributed on the surface of mesoporous MnO_2 ^{10,27}. The two peaks at high temperature ranging from 400 to 550°C are associated with coordinated NH_3 molecules originating from the Lewis acid sites, which may be caused by decomposition of nitrite-nitrate species which are formed due to oxidation of ammonia by MnO_2 ^{27,28}. Compared with mesoporous

MnO₂ and mesoporous Mn₂O₃, no Brønsted acid sites were obviously observed for bulk MnO₂. Due to Brønsted acid sites also play an important role in SCR reaction, which may be one of the reasons that the SCR reaction activity of mesoporous MnO₂ and mesoporous Mn₂O₃ is higher than bulk MnO₂^{28,29}. The NH₃-TPD spectra obtained from mesoporous Mn₂O₃ is similar with mesoporous MnO₂, which may be associated to the same morphologies. The difference of acid sites on the three catalysts may result from their specific structural features, leading to the distinction of the catalytic performance.

To investigate the reducibility of mesoporous MnO₂, mesoporous Mn₂O₃ and bulk MnO₂ catalysts in SCR reaction, the H₂-TPR patterns of are as shown in Figure 4b. For bulk MnO₂, three reduction peaks of bulk MnO₂ ranging from 350 to 600 °C can be observed, which attributes to correspond to the reduction of MnO₂ to Mn₂O₃, Mn₂O₃ to Mn₃O₄ and Mn₃O₄ to MnO, respectively^{25,29}. For mesoporous MnO₂, the reduction peak ranging from 200 to 600 °C is due to the reduction of MnO₂ to Mn₃O₄ and further reduction of Mn₃O₄ to MnO, which is in accordance with the previous study^{25,30}. As a comparison, the H₂-TPR peaks of mesoporous Mn₂O₃ show two reduction peaks ranging from 200 to 600 °C: the low temperature reduction peak centered at 360 °C is due to the reduction from Mn₂O₃ to Mn₃O₄ and the high temperature reduction peak centered at 540 °C is assigned to the further reduction of Mn₃O₄ to MnO, which is in good agreement with the previous report, which indicated that Mn₂O₃ sample undergo the stepwise reduction of Mn₂O₃ to Mn₃O₄, and Mn₃O₄ to MnO^{10,28}. Compared with bulk MnO₂, the first reduction peak of mesoporous MnO₂ and mesoporous Mn₂O₃ shifted to low temperature, implying their reduction potentials in low temperatures should be much higher than that of bulk MnO₂^{27,29}. The difference between bulk MnO₂ and the mesoporous manganese oxide could be explained considering a small size effect: the smaller particle size will result in the lower reduction temperature, thus, the reduction potentials in low temperatures will be stronger²⁹⁻³¹. Based on the average particles size calculated by XRD patterns, the average size of mesoporous MnO₂, mesoporous Mn₂O₃ and bulk MnO₂ are 7.2nm, 13nm and 36.4nm, respectively. Thus, the reduction potentials in low temperatures of mesoporous MnO₂ is strongest and the reduction potentials in low temperatures of bulk MnO₂ is weakest. For mesoporous MnO₂, the small size particles may be due to that the growth of MnO₂ particles occurred in the pore of KIT-6 template, thus, the mesoporous MnO₂ particles size will be strictly limited by the mesoporous channels of

KIT-6¹²⁻¹⁶. Moreover, the particles size of the bulk MnO₂ is much bigger than mesoporous MnO₂ due to the calcination growth. These results indicate that the ordered mesoporous channels changed the particles size and further improved the reduction potentials of samples in SCR removal NO.

To obtain the information about the oxidation states and the atomic compositions of manganese and the information about oxygen species on the catalyst surface, the XPS spectra of Mn 2p, O 1s of mesoporous MnO₂, mesoporous Mn₂O₃ and bulk MnO₂ are shown in Figure 5, which had been calibrated against the C 1s peak standardized at 284.6 eV³¹. From Figure 5a, two main peaks belong to Mn 2p_{3/2} and Mn 2p_{1/2} of mesoporous MnO₂, mesoporous Mn₂O₃ and bulk MnO₂ can be observed. After a peak-fitting deconvolution, the Mn 2p_{3/2} of mesoporous MnO₂ and bulk MnO₂ can be only separated into one peak with Mn⁴⁺ (642.1-642.2eV), and the corresponding peaks of mesoporous MnO₂ and bulk MnO₂ in Mn 2p_{1/2} can also be separated into one peak with Mn⁴⁺ (653.5-653.8eV), indicating that Mn⁴⁺ is the main valence state of Mn in MnO₂³². However, the the Mn 2p_{3/2} of mesoporous Mn₂O₃ can be separated into two peaks with Mn³⁺ (642.1 eV) and Mn⁴⁺ (642.4eV), and the corresponding peaks of Mn2p^{1/2} are located in 653.2 eV (Mn³⁺) and 654.2 eV (Mn⁴⁺)³³.

From Figure 5b, two kinds of surface oxygen species can be distinguished by performing a peak-fitting deconvolution. Peak at lower B.E. of 528.0-530.0 eV belongs to the surface lattice oxygen (O_β), and the peaks at higher B.E. of 531.0-532.0 eV can be assigned to the surface chemisorbed oxygen (O_α), such as the defect oxides or surface oxygen ions bonded to manganese in a low coordinated environment^{33,34}. The ratio of O_α/ (O_α+O_β) in mesoporous MnO₂ (47.02%) was much higher than that in bulk MnO₂. Because the surface chemisorbed oxygen is active in oxidation reaction, the higher O_α rate will be conducive to the reaction of SCR, which can be confirmed by following the results of SCR activity^{34,35}. The O_α rate between mesoporous MnO₂ and Mn₂O₃ is no significant difference, suggesting that the O_α rate has little effect on the difference in SCR activity between mesoporous MnO₂ and Mn₂O₃.

Binding energies and the percent of different valence states for manganese and oxygen determined from deconvoluted XPS spectra are as shown in Table 2. It is found that the Mn⁴⁺ is the predominant

ARTICLE

valence state of Mn. By the way, it can also be verified from the following SCR activity. From Table 2, the Mn^{4+} concentration of mesoporous MnO_2 is higher than mesoporous Mn_2O_3 , and the Mn^{4+} plays a key role in SCR activity and is preferable for SCR activity, in good agreement with the previous report^{28,32}. Therefore, that may be one of the reasons the NO removal efficiency of mesoporous Mn_2O_3 is lower than mesoporous MnO_2 .

3.2 SCR activity

As shown in Figure 6, the SCR removal activity of NO with different catalysts has been done, such as mesoporous MnO_2 , mesoporous Mn_2O_3 , bulk MnO_2 and commercial VWTi catalyst. As illustrated in Figure 6, only less than 20% NO conversion can be obtained below 150°C for VWTi. However, the NO conversion for VWTi can increase quickly to 98% at 300 °C. Moreover, the highest NO conversion for bulk MnO_2 is 58.35%, the 50% NO conversion below 200°C can be reach. From Figure 6, the NO conversion ratio with mesoporous MnO_2 is twice as bulk MnO_2 in the whole temperature window. For mesoporous MnO_2 , the NO conversion reach more than 97% in the temperature window ranging from 150 to 250 °C, and the highest NO conversion can be increased by up to 100% at 200 °C. Based on the results of N_2 adsorption-desorption, XPS, TPR and TPD, compared with bulk MnO_2 , the much higher NO conversion over mesoporous MnO_2 can be attributed to its huge specific surface area, more surface chemisorbed oxygen, high reducibility and strong acid sites^{10,31}. It also can be shown that the highest NO conversion of mesoporous Mn_2O_3 is 94.35% and the best active temperature also ranges from 150 to 250 °C, which is a little lower than mesoporous MnO_2 . Founded on the analysis of N_2 adsorption-desorption and XPS, it can be ascribed to the smaller specific surface area and the lower content of Mn^{4+} compared to the mesoporous MnO_2 . Therefore, it indicates that specific surface area and oxidation states of manganese can improve the SCR activity of manganese oxide⁹.

3.3 Effect of H_2O and GHSV

In practical, some fraction of water vapor exists in the air. Therefore, it is important to evaluate the effect of water vapor in the SCR reaction for mesoporous MnO_2 . We carried out the SCR reaction with the GHSV of 28000 h^{-1} in the existence of 5% H_2O to test the durability of the catalyst (Figure 7a). As can be seen, in the absence of 5% H_2O , mesoporous MnO_2 show a high and steady NO conversion of 99% in 200 °C. In the presence of 5% H_2O , the NO

conversion would decrease to 91% due to the blocking of some active sites on the catalyst surface^{31, 35}. After cutting off the H_2O inlet, the NO conversion over mesoporous MnO_2 rapidly recovered to 99%, which indicates a reversible inhibition effect of H_2O on the SCR activity.

As shown in Figure 7b, to further investigate the SCR activity under different reaction temperature and GHSV by using mesoporous MnO_2 as catalyst, NO conversion ratio has been valued in a wider reaction temperature from 100 to 350°C in the GHSV of 28000-100000 h^{-1} . It could be found that the NO conversion decreased with elevated GHSV, because their contact time becomes shorter and shorter²⁷. It is also shown obviously that the GHSV has little influence on SCR activity in the whole temperature window of 100-350 °C, and at GHSV of 53000 h^{-1} , the mesoporous MnO_2 still achieve more than 90% at low temperature ranging from 150 to 250 °C. And even at high GHSV of 100000 h^{-1} , the NO conversion can reach 90% at 200 °C. Noticeably, mesoporous MnO_2 still show more than 95% NO conversion at wide temperature window of 150-250 °C and higher GHSV of 28000 h^{-1} .

3.4 In situ DRIFT discussion

To further investigate the reaction mechanism, in situ DRIFT was conducted in Figure 8. In this experiment, the mesoporous MnO_2 was first treated with $\text{NO}+\text{O}_2/\text{Ar}$ for 30 min and then purged with Ar for 30 min. When NH_3 was introduced at 150 °C, the DRIFT spectra can be recorded as a function of time (Fig. 8a). After $\text{NO}+\text{O}_2$ adsorption, there are three nitrate species that was detected, which are the bands at 1623 cm^{-1} and at 1295 cm^{-1} corresponded to bridging nitrate, the band at 1580 cm^{-1} due to bidentate nitrate, and the band at 1545 cm^{-1} attributed to monodentate nitrate, respectively^{35,36}. After NH_3 was purged over mesoporous MnO_2 , the peak of bidentate nitrate is vanished rapidly because of its high reactivity, and the presence of the band at 1623 cm^{-1} which transformed to the higher band at 1624 cm^{-1} indicates the high stability of bridging nitrate because of its high stability^{36,37}. Meanwhile, a great of NH_3 species can be detected, such as hydrogen bond, coordination to an electron-deficient metal atom (Lewis acid site), dissociation of NH_3 with formation of NH_2 or NH groups, and formation of NH_4^+ at Brønsted acid sites. The features centered at 3160 and 3260 cm^{-1} were attributed to the stretching vibrations of weakly absorbed ammonia species³⁵. The band at 1031 cm^{-1} is caused by ammonia hydrogen bonding to the surface oxygen atoms of mesoporous MnO_2 , whereas the bands at 1430 and 1473 cm^{-1} are correlated to NH_4^+ ions formed

on Brønsted acid sites^{38,39}. A new band at 1340 cm^{-1} is quite different from adsorbed NOx and NH₃ species mentioned above, which assigned to the intermediate species from the combination of surface adsorbed NH₃ and NOx species⁴⁰. All the results indicated that the reaction between ammonia and nitrate species was unlikely to have occurred, except for the reaction between NO₂ and ammonia. And the coexistence of ammonia and nitrate species showed that NH₃ and NOx could be adsorbed over different active sites of the catalyst surface.

The in situ DRIFTS spectra of the reaction between NO+O₂ and pre-adsorbed NH₃ species on the catalyst at 150 °C is displayed in Figure 8b, which is conducted in reverse order compared with Figure 8a. The mesoporous MnO₂ were first treated with NH₃/Ar for 30min and then purged with Ar for 30 min. When NH₃ was introduced at 150 °C, the spectra were recorded at different time. After NH₃ adsorption, some NH₃ species are observed, including the band at 1625 cm^{-1} and 1193 cm^{-1} due to the symmetric and asymmetric deformation vibration of ammonia coordination to Lewis acid sites, the band at 1394 cm^{-1} correlated to NH₄⁺ ions formed on Brønsted acid sites. After NO+O₂ was purged over mesoporous MnO₂, the bands due to adsorbed NH₃ species decrease slightly and main nitrate species begin to form on the catalyst surface. The bands centered at 1625 and 1295 cm^{-1} are assigned to bridging nitrate and the bands at 1580 cm^{-1} is attributed to bidentate nitrate. Besides, a new band at 1340 cm^{-1} can be observed obviously, which assigned to the intermediate species from the combination of surface adsorbed NH₃ and NOx species. All these results indicate that both ionic NH₄⁺ and coordinate NH₃ can play important roles in reducing NO in SCR reaction.

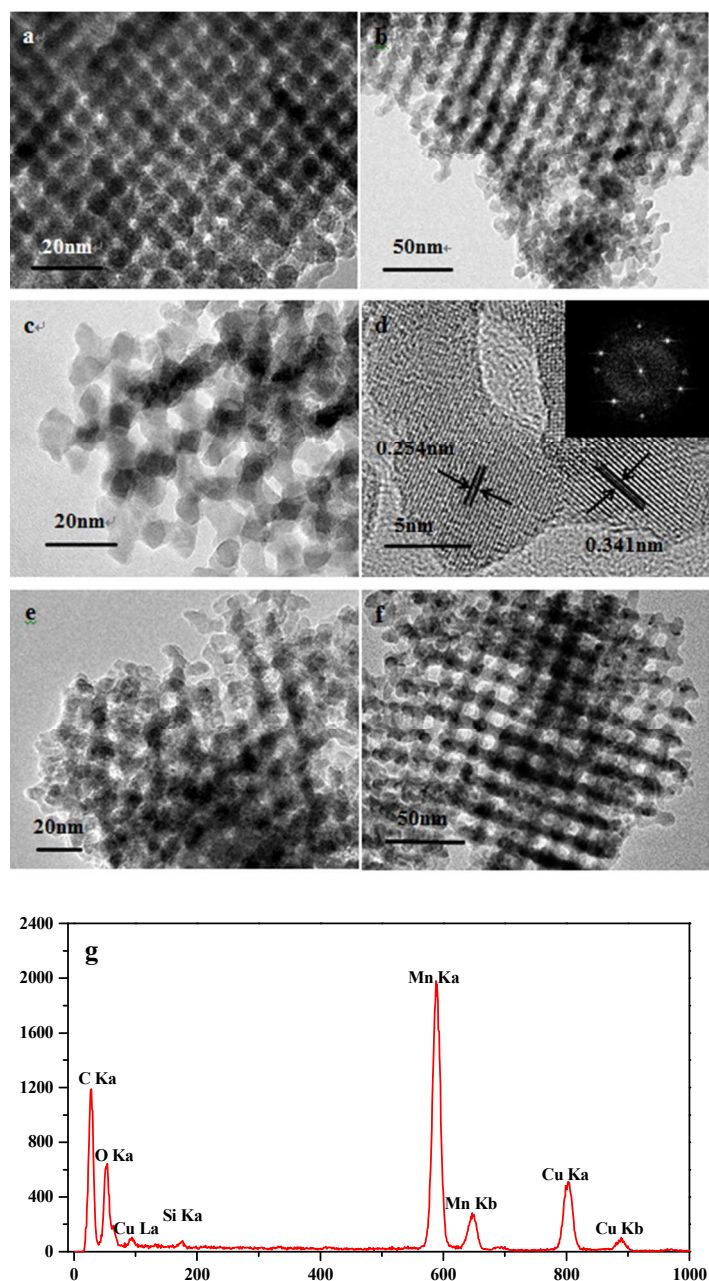


Figure 1. TEM images of KIT-6 (a), mesoporous MnO₂ (b,c), mesoporous Mn₂O₃ (e) and the used mesoporous MnO₂ (f), HRTEM image (d) of mesoporous MnO₂, and the energy spectrum analysis (EDS) (g) of mesoporous MnO₂.

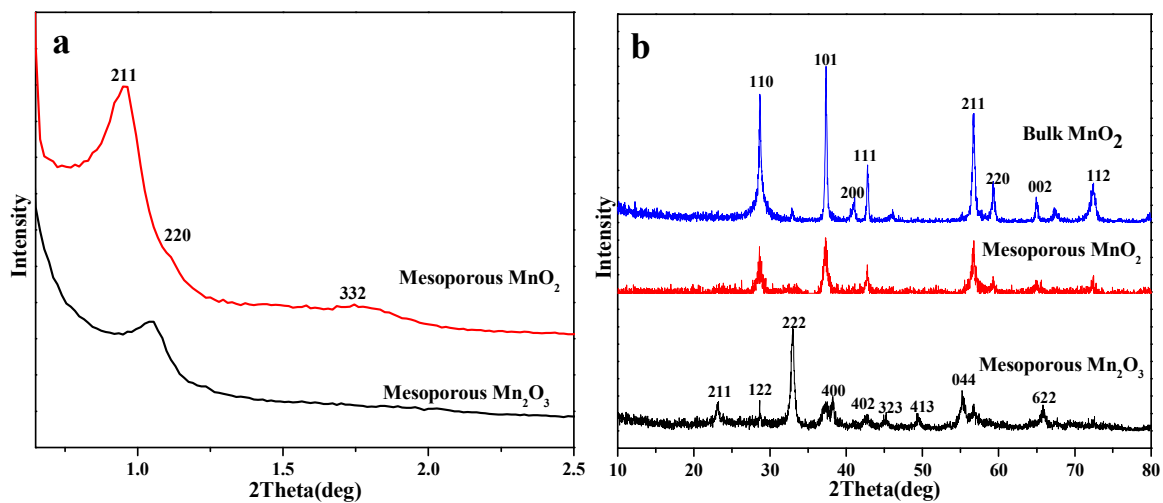


Figure 2. Low-angle XRD pattern of mesoporous MnO₂ and Mn₂O₃ (a), and wide-angle XRD pattern of mesoporous MnO₂, Mn₂O₃ and bulk MnO₂ (b)

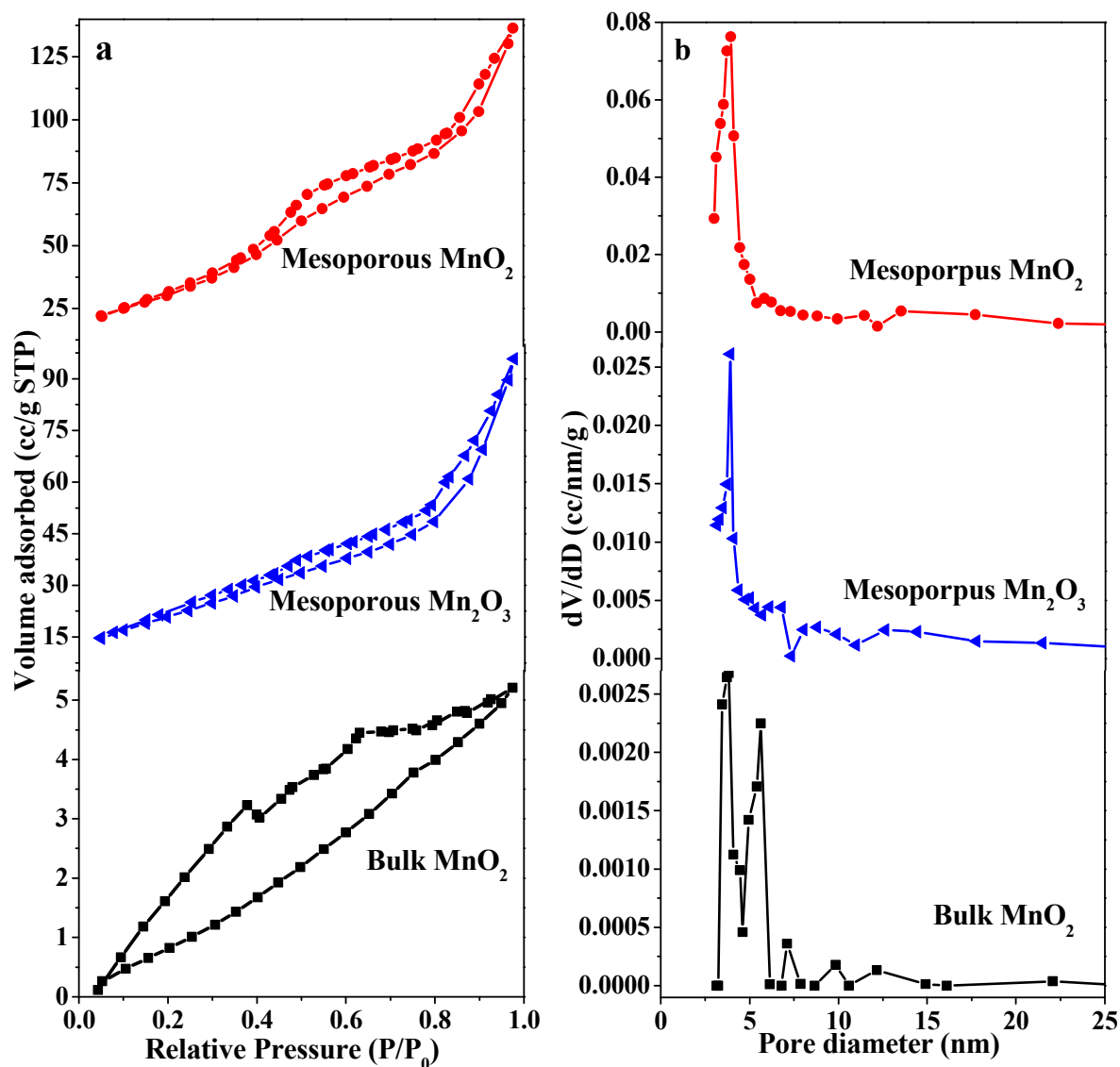


Figure 3. N₂ adsorption-desorption isotherms (a) and pore diameter distribution (b) of mesoporous MnO₂, mesoporous Mn₂O₃ and bulk MnO₂

Table 1. Specific area, pore volume, and pore diameter distribution of mesoporous MnO₂, mesoporous Mn₂O₃ and bulk MnO₂.

<i>materials</i>	<i>specific area (m²/g)</i>	<i>pore volume (cc/g)</i>	<i>pore diameter (nm)</i>
Mesoporous MnO ₂	116.668	0.203	3.882
Mesoporous Mn ₂ O ₃	78.724	0.068	3.866
Bulk MnO ₂	5.589	0.006	3.829

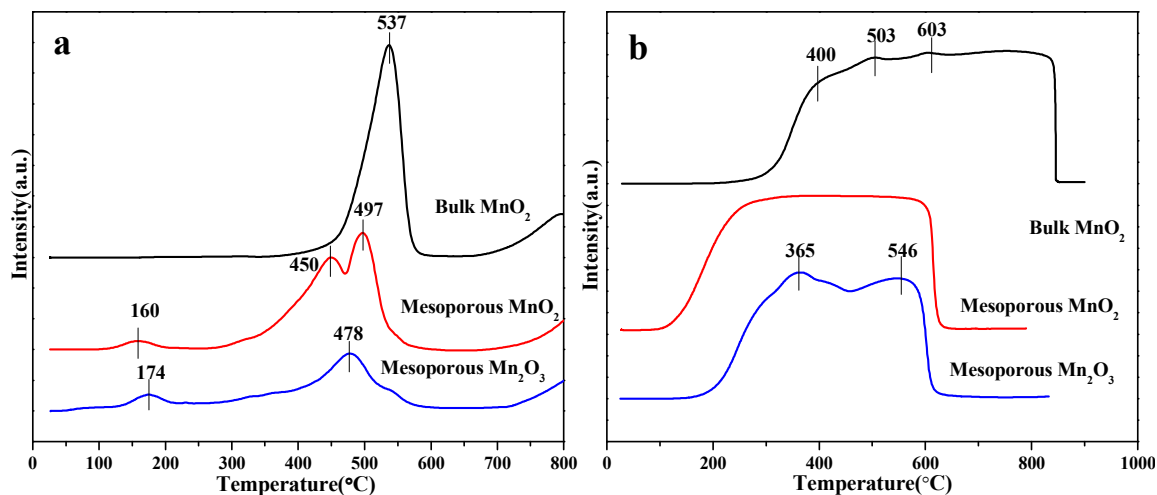


Figure 4. NH₃-TPD patterns (a) and H₂-TPR patterns (b) of mesoporous MnO₂, mesoporous Mn₂O₃ and bulk MnO₂

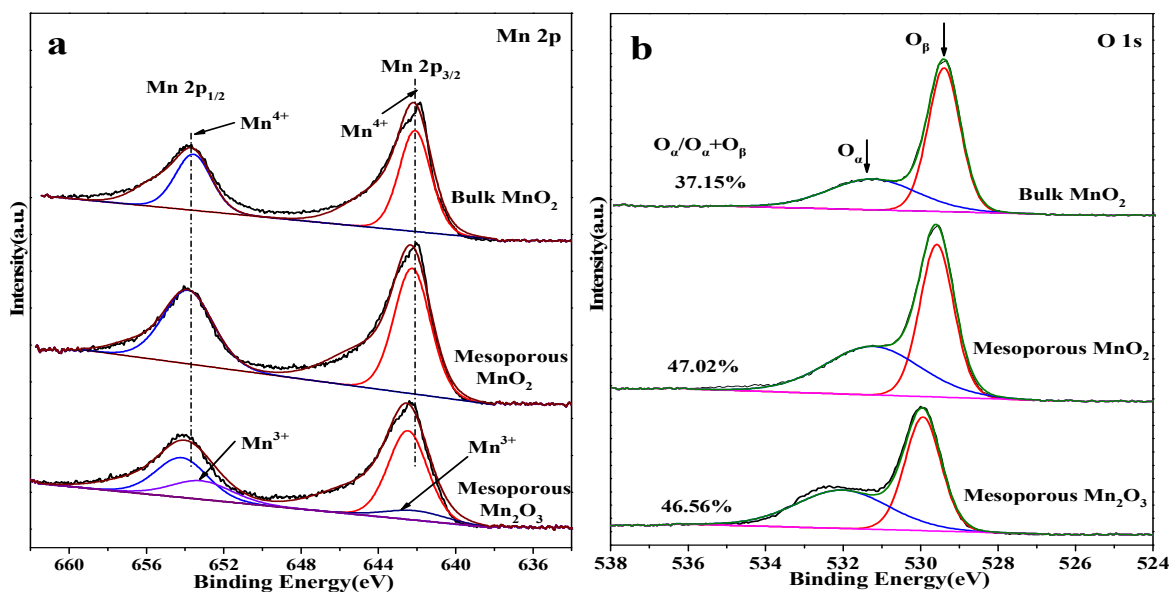


Figure 5. XPS spectrum of mesoporous MnO₂, mesoporous Mn₂O₃ and bulk MnO₂: (a) Mn2p, (b) O1s.

Table 2. Binding energies and the percent of different valence states for manganese and oxygen determined from deconvoluted XPS spectra.

Materials	Percent of valence state, % (binding energy, eV)					
	Mn ⁴⁺	Mn ⁴⁺	Mn ³⁺	Mn ³⁺	O _α	O _β
	2p _{3/2}	2p _{1/2}	2p _{3/2}	2p _{1/2}		
Mesoporous MnO ₂	55.24 (642.2)	44.76 (653.8)	--	--	47.02 (531.2)	52.98 (529.6)
Mesoporous Mn ₂ O ₃	48.17 (642.4)	28.35 (654.2)	5.45 (642.1)	10.67 (653.2)	46.56 (532)	53.44 (529.9)
Bulk MnO ₂	61.28 (642.1)	38.72 (653.5)	--	--	37.15 (531.3)	37.85 (529.5)

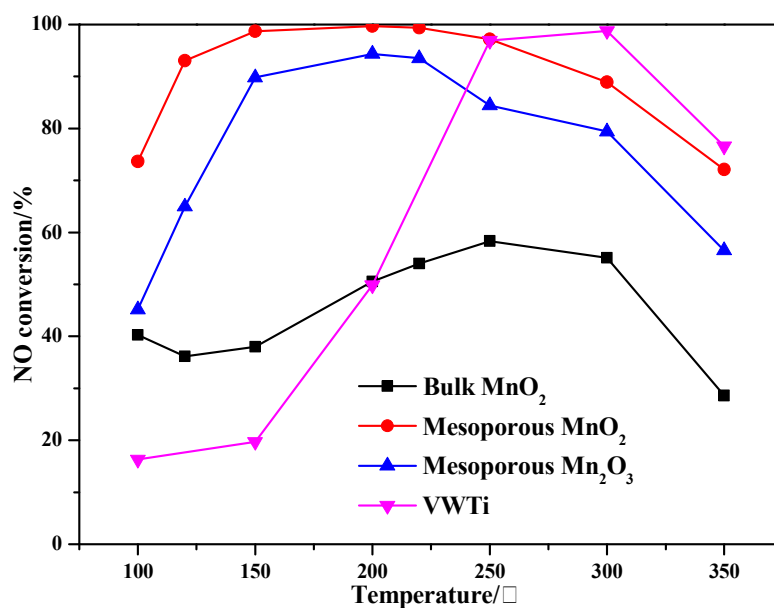


Figure 6. NO conversion of mesoporous MnO₂, mesoporous Mn₂O₃, bulk MnO₂ and VWTi under the conditions of 500 ppm NO, 500 ppm NH₃, 3% O₂, GHSV of 28,000 h⁻¹ and N₂ balance gas.

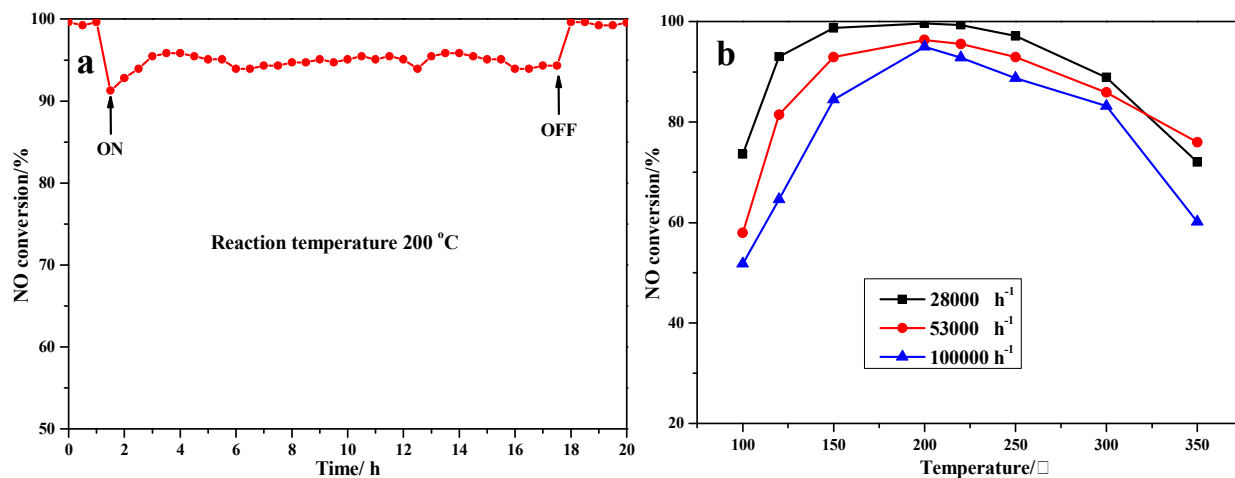


Figure 7. The effect of H₂O (a) and GHSV (b) on NO conversion for mesoporous MnO₂ at 200 °C. Reaction condition: 500ppmNO, 500ppmNH₃, 3%O₂, 5% H₂O (when used), and N₂ balance gas.

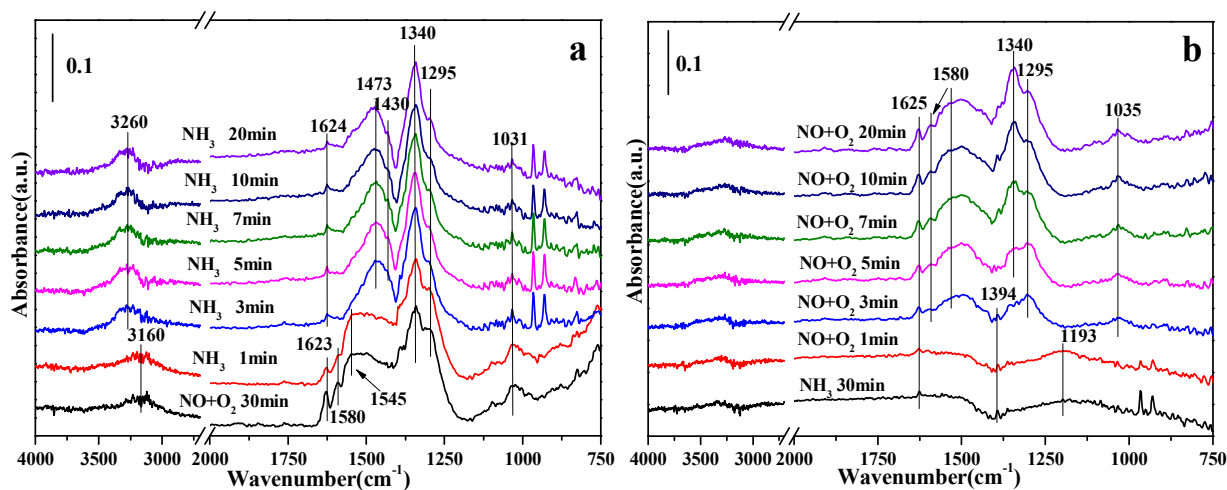


Figure 8. In situ DRIFT spectra of mesoporous MnO₂ between (a) NH₃ and adsorbed NO at 150 °C, (b) NO + O₂ and adsorbed NH₃ species at 150 °C.

4 Conclusions

In this manuscript, highly ordered mesoporous MnO₂ and Mn₂O₃ has been successfully prepared through nanocasting using KIT-6 as hard template and applied in SCR removal of NO with NH₃. The mesoporous MnO₂ could clean approximately 100% NO at wide window temperature from 150 to 250 °C. Mesoporous Mn₂O₃ and bulk MnO₂ were compared with mesoporous MnO₂ in order to illustrate the effect of mesostructure and oxidation state of manganese oxide on SCR reaction. It is found that the NO conversion of mesoporous MnO₂ is more than bulk MnO₂ due to its huge specific surface area, more surface chemisorbed oxygen, high reducibility and strong acid sites based on XPS, H₂-TPR, NH₃-TPD and DRIFT, which indicates that mesostructure can effect on the specific surface area, surface chemisorbed oxygen, reducibility and acid sites of catalyst and further influence the SCR reaction. On the other hand, the NO conversion of mesoporous MnO₂ is also higher than mesoporous Mn₂O₃, which can attribute to its more Mn⁴⁺.

Acknowledgements

The authors gratefully acknowledge the financial support provided by the National Natural Science Foundation of China (21377061), the Asia Research Center in Nankai University (AS1326), the Natural Science Foundation of Tianjin (12JCQNJC05800), and the Key Technologies R&D Program of Tianjin (13ZCZDSF00300) and the assistance provided by Dr. Raymond Seekell (University of Notre Dame) in the manuscript preparation and discussion.

Note and References

- S. J. Yang, C. X. Liu, H. Z. Chang, L. Ma, Z. Qu, N. Q. Yan, C. Z. Wang and J. H. Li, *Ind. Eng. Chem. Res.* 2013, 52, 5601-5610.
- Y. Peng, J. H. Li, L. Chen, J. H. Chen, J. Han, H. Zhang and W. Han, *Environ. Sci. Technol.* 2012, 46, 2864-2869.
- P. Li, Y. Xin, Q. Li, Z. P. Wang, Z. L. Zhang and L. Zheng, *Environ. Sci. Technol.* 2012, 46, 9600-9605.
- Z. M. Liu, Y. Yi, S. X. Zhang, T. L. Zhu, J. Z. Zhu and J. G. Wang, *Catal. Today* 2013, 216, 76-81.
- K. Zhuang, J. Qiu, F. S. Tang, B. L. Xu and Y. Fan, *Phys. Chem. Chem. Phys.*, 2011, 13, 4463-4469.
- D. Fang, J. L. Xie, D. Mei, Y. M. Zhang, F. He, X. Q. Liu and Y. M. Li, *RSC Adv.*, 2014, 4, 25540-25551.
- A. Patel, P. Shukla, J. L. Chen, T. E. Rufford, V. Rudolph and Z. H. Zhu, *Catal. Today* 2013, 212, 38-44.
- Z. H. Chen, F. R. Wang, H. Li, Q. Yang, L. F. Wang and X. H. Li, *Ind. Eng. Chem. Res.* 2012, 51, 202-212.
- F. Kapteljn, L. Sngoredjo and A. Andreml, *Appl. Catal. B: Environ.*, 1994, 3, 173-169.
- W. Tian, H. S. Yang, X. Y. Fan and X. B. Zhang, *J. Hazard. Mater.* 2011, 188, 105-109.
- B. Zhi, H. Ding, D. M. Wang, Y. Cao, Y. Zhang, X. Wang, Y. L. Liu and Q. S. Huo, *J. Mater. Chem. A*, 2014, 2, 2374-2382.
- Y. J. Sa, K. Kwon, J. Y. Cheon, F. Kleitz and S. H. Joo, *J. Mater. Chem. A*, 2013, 1, 9992-10001.
- Q. F. Li, L. X. Zeng, J. C. Wang, D. P. Tang, B. Q. Liu, G. N. Chen, and M. D. Wei, *ACS Appl. Mater. Interfaces* 2011, 3, 1366-1373.
- T. Waitz, T. Wagner, T. Sauerwald, C. D. Kohl and M. Tiemann, *Adv. Funct. Mater.* 2009, 19, 653-661.
- J. Rosen, G. S. Hutchings and F. Jiao, *J. Am. Chem. Soc.* 2013, 135, 4516-4521.
- M. Kundu, C. Ng, D. Y. Petrovykh and L. F. Liu, *Chem. Commun.*, 2013, 49, 8459-8461.
- J. P. Ma, Q. L. Cheng, V. Pavlinek, P. S. Saha and C. Z. Li, *New J. Chem.*, 2013, 37, 722-728.
- R. A. Chandru, S. Patra, C. Oommen, N. Munichandraiah and B. N. Raghunandan, *J. Mater. Chem.*, 2012, 22, 6536-6538.
- F. Kleitz, S. H. Choi and R. Ryoo, *Chem. Commun.*, 2003, 2136-2137.
- J. Y. Luo, J. J. Zhang and Y. Y. Xia, *Chem. Mater.* 2006, 18, 5618-5623.
- X. Z. Cui, J. Zhou, Z. Q. Ye, H. R. Chen, L. Li, M. L. Ruan and J. L. Shi, *J. Catal.* 2010, 270, 310-317.
- Y. Ren, A. R. Armstrong, F. Jiao and P. G. Bruce, *J. Am. Chem. Soc.* 2010, 132, 996-1004.
- Y. X. Liu, H. X. Dai, J. G. Deng, S. H. Xie, H. G. Yang, W. Tan, W. Han, Y. Jiang and G. S. Guo, *J. Catal.* 2014, 309, 408-418.
- F. Jiao, A. Harrison, A. H. Hill and P. G. Bruce, *Adv. Mater.* 2007, 19, 4063-4066.
- J. G. Deng, L. Zhang, H. X. Dai, Y. S. Xia, H. Y. Jiang, H. Zhang and H. He, *J. Phys. Chem. C* 2010, 114, 2694-2700.
- Y. F. Han, F. X. Chen, Z. Y. Zhong, K. Ramesh, L. W. Chen, and E. Widjaja, *J. Phys. Chem. B* 2006, 110, 24450-24456.
- C. Wang, L. Sun, Q. Q. Cao, B. Q. Hu, Z. H. Huang and X. F. Tang, *Appl. Catal. B: Environ.* 2011, 101, 598-605.
- Y. Wan, W. Zhao, Y. Tang, L. Li, H. Wang, Y. Cui, J. Gu, Y. Li and J. Shi, *Appl. Catal. B: Environ.* 2014, 148-149, 114-122.
- X. Tang, J. Li, L. Sun and J. Hao, *Appl. Catal. B: Environ.* 2010, 99, 156-162.
- A. Sultana, M. Sasaki and H. Hamada, *Catal. Today* 2012, 185, 284-289.
- B. Thirupathi and P. G. Smirniotis, *J. Catal.* 2012, 288, 74-83.
- C. Yu, G. Li, L. Wei, Q. Fan, Q. Shu and J. C. Yu, *Catal. Today* 2014, 224, 154-162.
- D. Zhang, L. Zhang, C. Fang, R. Gao, Y. Qian, L. Shi and J. Zhang, *RSC Adv.*, 2013, 3, 8811-8819.
- H. Chang, X. Chen, J. Li, L. Ma, C. Wang, C. Liu, J. W. Schwank and J. Hao, *Environ. Sci. Technol.* 2013, 47, 5294-301.
- A. Karami and V. Salehi, *J. Catal.* 2012, 292, 32-43.
- F. Liu and H. He, *J. Phys. Chem. C* 2010, 114, 16929-16936.
- M. Casapu, O. Krocher, M. Mehring, M. Nachttegaal, C. Borca, M. Harfouche and D. Grolimund, *J. Phys. Chem. C* 2010, 114, 9791-9801.
- W. C. Wang, G. McCool, N. Kapur, G. Yuan, B. Shan, M. Nguyen, U. M. Graham, B. H. Davis, G. Jacobs, K. Cho and X. H. Hao, *Science* 2012, 337, 832.
- D. S. Zhang, L. Zhang, L. Y. Shi, C. Fang, H. R. Li, R. H. Gao, L. Huang and J. P. Zhang, *Nanoscale*, 2013, 5, 1127-1136.
- L. Chen, J. Li and M. Ge, *Environ. Sci. Technol.* 2010, 44, 9590-9596.

ARTICLE

^a College of Environmental Science and Engineering, Key Laboratory of Environmental Pollution Process and Environmental Criteria, Nankai University, Tianjin 300071, P. R. China;

^b Department of Chemistry and Biochemistry, University of Notre Dame, Notre Dame, Indiana 46556, United States;

^c Department of Chemistry, Tianjin University, Tianjin 300072, P. R. China.